13th International Symposium on Turbulence and Shear Flow Phenomena (TSFP13)
Montreal, Canada, June 25-28, 2024

PRIMARY ATOMIZATION AND TURBULENT/NON-TURBULENT INTERFACE IN LIQUID ROUND JET FLOW

Seongdeuk Moon
School of Mechanical Engineering
Pusan National University
Busan 46241, Korea
sd9806@pusan.ac.kr

Jinyul Hwang
School of Mechanical Engineering
Pusan National University
Busan 46241, Korea
jhwang@pusan.ac.kr

ABSTRACT

When a stream of liquid is injected into a stationary gas, it leads to the atomization of the liquid jet, breaking the liquid column into numerous droplets. While the atomization of the liquid jet plays an important role in combustion systems, the multiscale complexity of the atomization phenomena leaves many questions unanswered, particularly regarding their interactions with turbulent flows. During atomization, a turbulent/non-turbulent interface (TNTI) also develops, which governs the mass and momentum exchange across the turbulent jet. Owing to a broad range of turbulent motions along TNTI, atomization phenomena become significantly more complex. This study explores the interaction between TNTI behaviour and primary atomization in a liquid round jet flow by conducting a large-eddy simulation of a liquid round jet. The TNTI location is obtained by assessing the probability density function (PDF) of vorticity magnitude. Our examination focuses on the entrainment phenomena near TNTI, specifically nibbling and engulfment processes, and their influence on primary atomization. To investigate this effect, the droplets are classified into two groups: one is near the TNTI and others are far from the TNTI. A significant number of droplets are located close to the TNTI. In addition, the number of droplets increases when the convoluted length of TNTI increases. With increasing enstrophy flux along the TNTI, the length scales of droplet decrease. Moreover, when inward propagation of the TNTI is dominant, it leads to a higher incidence of smaller droplets. These findings enhance the understanding of the interaction between primary atomization and TNTI dynamics, associated with the multiscale phenomena of entrainment.

INTRODUCTION

The phenomenon of liquid jet atomization occurs when the liquid exits a nozzle, encounters a stationary gas, and becomes unstable, separating into ligaments and droplets. This atomization of the liquid jet is a crucial step in many combustion systems. Liquid jet atomization is a complex phenomenon, and thus the associated mechanisms have not been fully elucidated (Shinjo et al., 2010). Therefore, in-depth research is essential to further understand the underlying physics of this phenomenon.

Primary breakup is the process where ligaments and droplets form from the liquid core. These ligaments and droplets continue to split into finer droplets due to aerodynamics interactions, referred to as secondary breakup. The effectiveness of primary breakup significantly influences the quality of atomization. The atomization of a liquid jet is a complex process, which can be affected by internal turbulent flow, cavitation, and aerodynamic effects. Among these, turbulence has a direct and indirect impact on the atomization process. The primary source of initial perturbation on the jet surface stems from turbulent fluctuations in the liquid jet.

In recent decades, there has been a significant endeavour regarding the analysis of turbulence in multiphase flows. Wu & Faeth (1992, 1993) investigated droplet characteristics during primary breakup initiation and found that the droplets generated in primary breakup are on the order of the inertial subrange scale. They argued that turbulent kinetic energy in the liquid jet surpasses surface tension energy at the liquid/gas interface, leading to droplet formation during primary breakup. The Kelvin-Helmholtz instability occurring at the liquid/gas interface facilitates the development of spanwise vorticity waves forming coherent vortices. These vortices transition into hairpin structures characterized by streamwise legs rotating in opposite directions (Bernal & Roshko, 1986). Jarrahbashi & Sirignano (2014) demonstrated the correlation between the mechanisms of lobe and ligament and the enhancement of streamwise vorticity. While it is anticipated that gas-phase turbulence influences the atomization breakup process, an in-depth understanding of the influence of turbulence is still lacking.

In turbulent jet flows, the turbulent region is encompassed by an irrotational region (a non-turbulent region). The boundary separating these two regions is called the turbulent/non-turbulent interface (TNTI). This interface is significantly deformed with the spreading of the turbulent region and also contains a wide range of scales. The characteristics of the flow near the TNTI have been explored by analysing conditional statistics according to the distance from the TNTI. These investigations have revealed that the TNTI has two thin layers, comprising a laminar superlayer where viscous effects dominate vorticity diffusion, and a turbulent sublayer where the inviscid effects dominate the enstrophy production (Corrisin & Kistler, 1955; Bisset et al., 2002).

Across the TNTI, turbulent entrainment occurs. This is the mechanism by which the non-turbulent flow moves into the turbulent region and becomes a part of the turbulent region. This entrainment process governs the exchange of mass, momentum, and scalar quantities through the TNTI with the surrounding fluid. There are two typical processes that attribute entrainment known as nibbling and engulfment (da Silva et al., 2014). Nibbling is a small-scale entrainment where viscous process occurs along the interface. Engulfment is the process of large-scale entrainment, where large blobs of irrotational fluid are absorbed into the turbulent flow before becoming vortical. Understanding these two processes is crucial for comprehending the TNTI dynamics and the associated entrainment process. There is some debate over which mechanism dominates. Engulfment was thought to predominantly govern the entrainment process (Dahm & Dimotakis, 1987). With advancements in data resolution, it has been noted that the

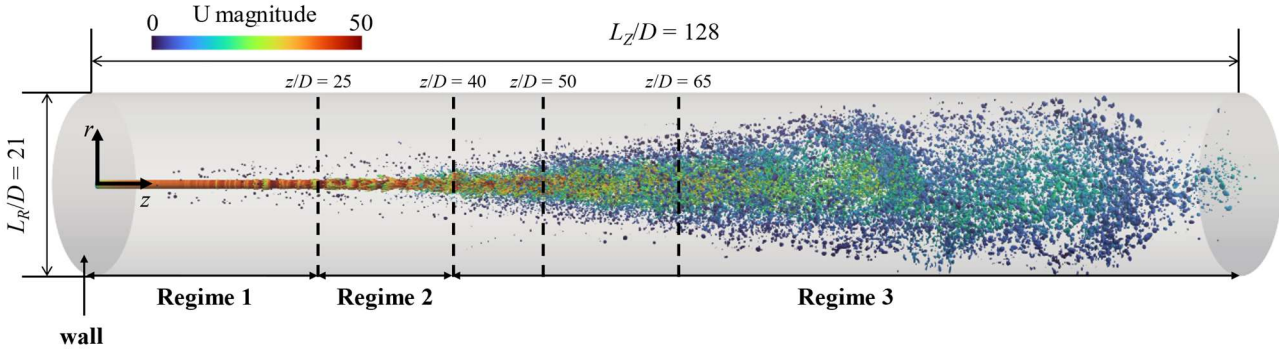

Figure 1. Illustration of the computational domain and the liquid jet atomization. Isosurfaces of liquid phase, α = 0.2, in the instantaneous flow field. The colour indicates the velocity magnitude. The breakup phenomenon consists of three regimes based from the figure 2. The Flow field data between 50 and 65 nozzle diameters in regime 3 is used.

contribution of large-scale motions is reported to be less than 10% (Westerweel et al., 2009). Recent research suggests that the dominant mechanism for jets is the nibbling mechanism. One of the difficulties in answering this ongoing question lies in objectively distinguishing between the engulfment and nibbling mechanisms.

To understand the primary atomization process, it is essential to comprehend the exchange of momentum between the ambient gas and the liquid jet. While previous studies (Zhou et al., 2021) have shown the relation between atomization and turbulence, there is a lack of analysis regarding the effect of turbulence on primary atomization in terms of entrainment through TNTI. In the present study, therefore, we aim to elucidate the relationship between TNTI behaviour and primary atomization by focusing on the entrainment phenomenon. Here, we demonstrate how the number of droplets varies depending on the distance from TNTI, and the convoluted length of TNTI. We find that droplets around TNTI, where inward propagation of the interface dominates, tend to be smaller in size compared to those in areas where outward propagation is predominant.

NUMERICAL DETAILS

To analyse the relationship between TNTI behaviour and primary atomization, we performed a large-eddy simulation of a liquid round jet flow using the volume-of-fluid solver, InterFOAM, in OpenFOAM. This solver solves the continuity equation, the momentum equation, and the phase continuity equation for the incompressible flow.

$$\frac{\partial \rho}{\partial t} + \frac{\partial (\rho u_i)}{\partial x_i} = 0. \quad (1)$$

$$\frac{\partial (\rho u_i)}{\partial t} + \frac{\partial}{\partial x_j}(\rho u_i u_j) = -\frac{\partial p}{\partial x_i} + \frac{\partial}{\partial x_j}(\mu \frac{\partial u_i}{\partial x_j}) + \rho g_i + f_{\sigma i} \quad (2)$$

$$\frac{\partial \alpha}{\partial t} + \nabla \cdot (\alpha u_i) = 0. \quad (3)$$

Fluid density and viscosity is defined as

$$\rho = \alpha \rho_l + (1-\alpha)\rho_g \quad (4)$$

$$\mu = \alpha \mu_l + (1-\alpha)\mu_g \quad (5)$$

where α is the volume fraction of the liquid phase in a cell. Hence, $\alpha = 1$ denotes the liquid phase, and $\alpha = 0$ indicates the gas phase. The subscripts l and g denote the liquid and gas phases, respectively. The volume fraction between 0 and 1 indicates the interface between the liquid and gas phases.

The injection is from a nozzle with a diameter of $D = 90\mu m$, where the inlet velocity profile is uniform at 50m/s with a flat hat profile. Here, z, r, and θ denote the axial, radial, and azimuthal directions, and u_z, u_r, and u_θ are the corresponding velocity components, respectively. The computational domain extends over a space given by $L_R \times Lz = 21D \times 128D$. The original number of grids is given by $N_z \times N_r \times N_\theta = 768 \times 75 \times 100$. In addition, to accurately capture the primary atomizaton, we employed an adaptive refinemesh. Here, the finest resolution is $\Delta z = 3.75\mu m$ and a level of refinemesh is set to 2 ($\Delta z = L/4$; L is original grid size) in liquid fraction regions. The flow condition for the atomization is described in table 1, which is consistent with the case 3 in Trujillo et al., (2018).

Table 1. The descriptions under the current simulation. Here $Oh = We^{1/2}/Re$ where $Re = U_e D/\nu_l$ and $We = \rho_l U_e^2 D/\sigma$.

Reynolds number	Re	6520
Liquid kinematic viscosity	ν_l	6.9×10^{-7} m^2/s
Gas kinematic viscosity	ν_g	3.76×10^{-7} m^2/s
Liquid density	ρ_l	688.03 kg/m^3
Gas density	ρ_g	50 kg/m^3
Coefficient of surface tension	σ	0.02 kg/s^2
Weber number	We	7740
Ohnesorge number	Oh	1.358×10^{-2}
Jet exit velocity	U_e	50 m/s

RESULTS AND DISCUSSION

Figure 1 illustrates the computational domain of the current simulation. In the figure, the isosurfaces denote the liquid fraction of α = 0.2 and are coloured by the velocity magnitude. As seen, the liquid column breaks into smaller droplets, and particularly as it progresses in the flow direction, more droplets are formed. From the region of $z/D > 40$, it can be seen that the liquid jet has undergone complete fragmentation. This behaviour can be further quantified by defining the mass flux of the interfacial region and the liquid region ($\dot{m}_\Gamma$ and $\dot{m}_L$) at a given cross-stream plane (Desantes et al., 2006):

$$\dot{m}_\Gamma(z,t) = \int_{A_z} \rho_l(r,t) u_z(r,t) \chi_\Gamma(r,t) dS, \quad (6)$$

$$\dot{m}_L(z,t) = \int_{A_z} \rho_l(r,t) u_z(r,t) \chi_L(r,t) dS, \quad (7)$$

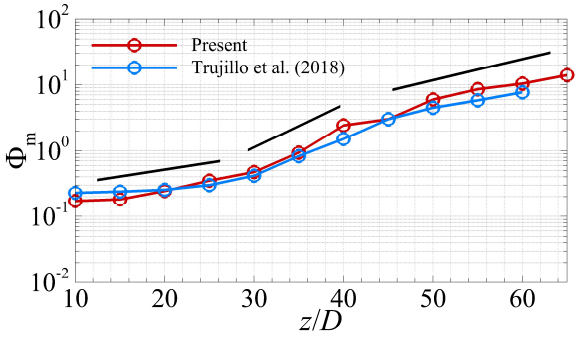

Figure 2. Variation of normalized mass flow rate along the streamwise direction. Here, the red line indicates present data and the blue line is the data of Trujillo et al. (2018)

where the area of the cross-stream plane is indicated by A_z. Here, χ_Γ and χ_L represent the indicator functions, representing the interfacial area and the liquid region at the cross-stream plane, respectively. The conditions are $0.05 < \alpha(r, t) < 0.95$ and $\alpha(r, t) > 0.95$ respectively. Hence, we can define the normalized mass flow $\Phi_m(z) \equiv \langle \dot{m}_\Gamma / \dot{m}_L \rangle$, indicating the momentum transfer across the interface. Here, the angled brackets denote the ensemble average. In figure 2, the profile of $\Phi_m(z)$ shows three distinct slopes. According to this fact, the breakup phenomena in figure 1 consist of three regimes. The initial regime ($< 25D$) corresponds to the region with the lowest slope and pertains to the emergence of initial instabilities along the jet column surface. Such instabilities lead to the surface fragmentation of the jet, while the core of the jet retains its shape. In the second regime ($25–40D$), the jet core begins to undergo primary atomization, leading to a notable increase in the momentum transfer between the gas and liquid phases. In the third regime ($> 40D$), such momentum transfer is enhanced, which in turn leads to a decrease in the velocity between the liquid and gas phases. This also affects the formation of fine liquid and gas phases. According to this observation, we analyse the flow field data ($50–65D$) in the third regime, because we anticipate that the interaction between the entrainment of the gas phase and the primary atomization amplifies.

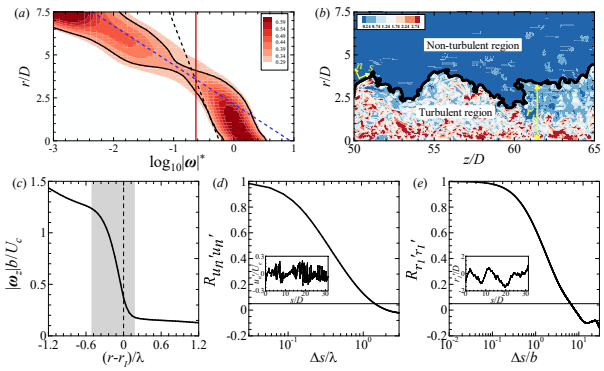

Figure 3. (*a*) PDF of the normalized vorticity magnitude $\log_{10}|\omega|^*$. The red vertical line indicates $|\omega|^* = 0.24$, the black dashed line denotes the lowest level of the PDF, and the blue dashed line corresponds to the ridge of the contour. (*b*) Normalized vorticity magnitude contours in the *r*-*z* plane. Here, the white solid line denotes the TNTI. (*c*) Conditional mean profile of the spanwise vorticity $|\omega_z|$ as a function of the distance from r_I. (*d*) Two-point correlation of u_n'. The inset shows signal of u_n' along the TNTI. (*e*) Two-point correlation of r_I'. The inset shows signal r_I' along the TNTI.

The detection of TNTI can be achieved through various methods such as turbulent kinetic energy, enstrophy, passive scalar, and vorticity magnitude (da Silva et al., 2014). In the present work, the vorticity magnitude is used to identify the TNTI; i.e., $|\omega|^* = |\boldsymbol{\omega}|/\omega_{rms}$ where ω_{rms} is taken at the centre of the jet. Figure 3(*a*) illustrates the probability density function (PDF) of $\log_{10}|\omega|^*$. The vorticity level significantly varies in the radial direction. There is a band connecting the turbulent and non-turbulent regions. The dashed black line represents the inclination of the lowest PDF contour, indicating a reduction in vorticity. The dashed blue line traces the centre of band within the outer intermittent flow region. The vorticity threshold, $|\omega|_{th}^* = 0.24$, is determined at the point where these two lines intersect (Lee et al., 2017).

Figure 3(*b*) displays the normalized vorticity magnitude in the instantaneous flow field over the range ($50–65D$). Within this subdomain, note that the microscale Reynolds number of the jet is $Re_\lambda = 373$ ($Re_\lambda = \overline{u'_{rms}}\lambda / \nu_l$) where λ is the Taylor microscale and $\overline{u'_{rms}}$ is the root mean square of u' at the center. In this figure, the black line represents the TNTI, distinguishing between the turbulent and non-turbulent regions. The strong vorticity magnitude is observed within the turbulent region while the magnitude significantly drops near the TNTI.

To examine this behavior further, we compute the radial variation of the spanwise vorticity (ω_z) with respect to the TNTI location (r_I) in figure 3(*c*). Here, b and U_c is jet half-width and center velocity, respectively. As seen, the vorticity diminishes on the non-turbulent side of the interface and exhibits a significant jump at the interface, which indicates the existence of a strong vortex sheet near the interface. These findings are related to a thin shear layer (or turbulent sublayer); the thickness of the shear layer is approximately 0.68λ, denoted by the shaded region in figure 3(*c*), which is similar to that found in the previous works (Chauhan et al., 2014; Borrell and Jiménez, 2016).

In inset of figure 3(*d*), the interface-normal velocity (u_n) is obtained by taking the inner product of the streamwise velocity ($u_{z,I}$) and radial velocity ($u_{r,I}$) at the interface and of the normal vector $\boldsymbol{n}$; i.e., $u_n = \boldsymbol{u}_I \cdot \boldsymbol{n}$ where $\boldsymbol{u}_I$ and $\boldsymbol{n}$ are the velocity vector at the interface and the interface-normal unit vector, respectively. Here, $\boldsymbol{n}$ is determined as $\boldsymbol{n} = -\nabla|\boldsymbol{\omega}|/|\boldsymbol{\omega}|$ in figure 3(*b*). The fluctuating velocity component is defined as $u_n' = u_n - \overline{u_n}$. It is clear that the signal of u_n is related to small scale (or nibbling) along the TNTI. The inset in figure 3(*e*) depicts the instantaneous interface height fluctuation (r_I') against the distance s along the interface, revealing that the variation of the interface height possesses a large-scale feature (or engulfment).

To statistically measure these small and large scales along the TNTI, we compute the two-point correlation of u_n' and r_I' (Chauhan et al., 2014; Yang et al., 2016) in figure 3(*d, e*). In figure 3(*d*), the two-point correlation is 0.05 at $\Delta s = 1.4\lambda$, representing the length scale of the nibbling motion, consistent with the findings of Mistry et al. (2019). Figure 3(*e*) plots the auto-correlation of r_I' along TNTI. This figure reveals a large-

scale feature, aligning with our visual observations; the correlation approaches 0.05 at $\Delta s = 6.5b$. These observations underscore the multi-scale nature of the TNTI and imply that the rate of increase in Φ_m (figure 2), which indicates the enhanced atomization process, is related to the entrainment phenomena of TNTI.

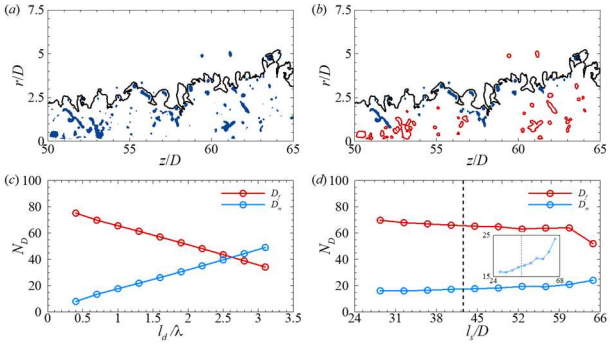

Figure 4. (a) TNTI (black line) and droplets (blue) in the instantaneous flow field. (b) Droplets filtered based on size, larger than $2\Delta z$ and $2\Delta r$ in each direction, are depicted; the blue contour highlights droplets near the TNTI (D_n), while the red contour outlines droplets far from the TNTI (D_f). (c) Number of droplets (N_D) with respect to l_d/λ. (d) Histogram of N_D with respect to the convoluted length of TNTI. The black dashed line is the average length of TNTI. The inset shows the variation of D_f.

Figure 4(a) depicts the TNTI and droplets in a snapshot of the flow field. We extract individual droplets using the structure identification method of previous works (Hwang & Sung 2018; Hwang & Sung 2019; Hwang et al., 2020). Using this approach, we can label all the individual droplet regions in instantaneous flow fields and measure the morphological information of each structure. Before examining the droplets, we filter out droplets whose sizes are less than two grid cells in both z and r directions (figure 4b) to exclude artificial droplets due to grid resolutions. To analyze the relation between the primary atomization and the TNTI, droplets are classified into two groups; one is near the TNTI and the others are far from the TNTI, based on the distance from the TNTI location of each droplet (l_d). Here, l_d is defined as the closest distance from the center of the rectangle surrounding the droplet to the TNTI location. Hence, droplets with $l_d < \alpha\lambda$ are considered as D_n, whereas those with $l_d > \alpha\lambda$ (D_f) are located far from the TNTI (α is constant). In figure 4(b), we classify D_n and D_f (blue and red contours) from figure 4(a) when $\alpha = 1$. In other words, D_n indicates the droplets where the distance from the TNTI location is on the order of the turbulent sublayer thickness and can be considered as the droplets associated with TNTI behaviour.

To quantitatively analyze the droplets near the TNTI, figure 4(c) displays the mean number of droplets (N_D) for D_n and D_f with respect to l_d/λ (= α). As observed, N_D for D_n increases with increasing α, while N_D for N_f decreases. At $l_d = 2.6\lambda$, N_D for D_f exceeds half of the total number of droplets. Interestingly, at $l_d = \lambda$, corresponding to the order of the turbulent sublayer thickness (figure 3c), N_D for D_n accounts for 21.2% of the total droplets. Given that the Taylor microlength scale is very small compared to the jet half-width ($\lambda = 0.23b$), a significant number of droplets are distributed very close to the TNTI, and it is speculated that these are influenced by the dynamics of the TNTI. Note that the droplets within $l_d/\lambda < 1$, in figure 4(b), constitute 43.5% of the total droplets, which is significantly higher than the mean fraction (≈ 21.2 %). In addition, the length of the TNTI in figure 4(b) is $3.55L_{zs}$, where L_{zs} is the subdomain length (= $15D$), representing a highly convoluted interface. This observation also confirms our speculation that the atomization process could be affected by TNTI dynamics.

To confirm this effect, we plot the N_D for D_n ($l_d/\lambda < 1$) and D_f ($l_d/\lambda > 1$) relative to the convoluted length of TNTI in figure 4(d). As observed, N_D for D_n increases with increasing l_s/D, while N_D for D_f decreases. At $l_s \approx 64.7D$ (= $4.3L_{zs}$), where the convoluted length of TNTI is considerably long, N_D for D_n accounts for 31.6% of the total droplets. On the other hand, at $l_s \approx 28.4D$ (=$1.9L_{zs}$) which has a shortly convoluted length of TNTI, N_D for D_n constitutes 18.7% of the total droplets. This investigation suggests atomization interacts with both large-scale engulfment and small-scale nibbling that contribute to the increased length of TNTI.

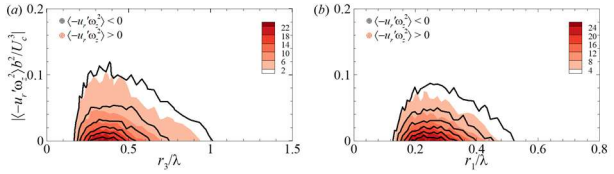

Figure 5. The joint PDFs of the characteristic length of droplet (r_3 and r_1) and the enstrophy flux. The color and black line contours correspond to the inward propagation and outward propagation, respectively.

To define the characteristic length of a droplet, we apply the box counting method (Liebovitch et al. 1989). Moisy & Jiménez (2004) used this method for analyzing the geometrical features of turbulence structures. In this context, the longest length scale of a droplet (r_3) corresponds to the longest dimension of the smallest box that can enclose the droplet, while the smallest length scale (r_1) corresponds to the length of the largest cube that fits entirely inside the droplet.

At the interface, the tangential component of the vorticity is dominant (Bisset et al., 2002). This can be quantified by the enstrophy flux $\langle -u_r'\omega_z^2 \rangle$ near the TNTI, indicating the transport of vorticity by entrainment (Westerweel et al., 2009). Figure 5(a, b) displays the joint PDF, which is presented to verify the relationship between the enstrophy flux and the characteristic lengths of D_n. The enstrophy flux is obtained by conditionally averaging the enstrophy flux along the interface, where the distance from the droplet is within λ. The color and black line contours correspond to the inward propagation ($\langle -u_r'\omega_z^2 \rangle > 0$) and outward propagation ($\langle -u_r'\omega_z^2 \rangle < 0$), respectively. The charateristic lengths (r_1 and r_3) of D_n are observed to have length on the order of λ. As the value of the enstrophy flux increases, it is observed that the overall size of droplets decreases. Additionally, with higher enstrophy flux values, inward propagation tends to produce smaller droplets compared to outward propagation. This suggests that droplets near the TNTI undergo significant momentum transfer due to entrainment, resulting in more vigorous primary atomization and subsequently producing smaller droplets.

In future research, we will investigate the relationship between the entrainment governed by small scales along TNTI and the droplet generation. The local entrainment velocity, which represents the enstrophy propagation velocity relative to the interface, can be decomposed into the inviscid and viscous components (Holzner & Lüthi 2010). In particular, the viscous

component, which is associated with small scales, depends on the local interface shape and governs the local entrainment velocity (Yang et al., 2019). In this regard, we will examine the influence of small-scale turbulence along the TNTI (i.e., nibbling) on primary atomization.

CONCLUSIONS

We investigate the influence of TNTI behaviour on the primary atomization in a liquid round jet. By extracting droplet regions in the instantaneous flow field, we classify them into two groups: one is near the TNTI and the others are far from the TNTI, based on the distance corresponding to the order of turbulent sublayer thickness. A number of droplets are found close to the TNTI, especially as the convoluted length of the TNTI increases, leading to a higher number of droplets. We also examine the joint PDF of the characteristic lengths of droplets and the enstrophy flux along the interface to explore the influence of entrainment in primary atomization. We observe that the size of droplets diminishes as the enstrophy flux increases. Furthermore, with increasing enstrophy flux, inward propagation of TNTI generally results in smaller droplets than outward propagation. Our results demonstrate the possible interaction between primary atomization and TNTI dynamics and suggest that primary atomization could be modulated by turbulent motions along TNTI.

ACKNOWLEDGEMENTS

This work was supported by a National Research Foundation of Korea (NRF) grant funded by the Korea government (MSIT) (Grant No. RS-2023-00211896 and Grant No. 2022M3H4A3095288).

REFERENCES

J. Shinjo and A. Umemura, 2010, "Simulation of liquid jet primary breakup: Dynamics of ligament and droplet formation", *International Journal of Multiphase Flow*, Vol. 36, pp. 513-532.

P.-K. Wu, L.-K. Tseng and G. M. Faeth, 1992, "Primary breakup in gas/liquid mixing layers for turbulent liquids", *Atomization and sprays*, Vol. 2, pp. 295-317.

P.-K. Wu and G. M. Faeth, 1993, "Aerodynamic effects on primary breakup of turbulent liquids", *Atomization and Sprays*, Vol. 3, pp. 265-289.

L. Bernal and A. Roshko, 1986, "Streamwise vortex structure in plane mixing layers", *Journal of Fluid Mechanics*, Vol. 170, pp. 499-525.

D. Jarrahbashi and W. Sirignano, 2014, "Vorticity dynamics for transient high-pressure liquid injection", *Physics of Fluids* ed., Vol. 26, pp.

S. Corrsin and A. L. Kistler, 1955, "Free-stream boundaries of turbulent flows", *NACA Tech*, Vol. pp. 120-130.

D. K. Bisset, J. C. Hunt and M. M. Rogers, 2002, "The turbulent/non-turbulent interface bounding a far wake", *Journal of Fluid Mechanics*, Vol. 451, pp. 383-410.

C. B. da Silva, J. C. Hunt, I. Eames and J. Westerweel, 2014, "Interfacial layers between regions of different turbulence intensity", *Annual Review of Fluid Mechanics*, Vol. 46, pp. 567-590.

W. Dahm and P. Dimotakis, 1987, "Measurements of entrainment and mixing in turbulent jets", *AIAA journal*, Vol. 25, pp. 1216-1223.

J. Westerweel, C. Fukushima, J. M. Pedersen and J. C. Hunt, 2009, "Momentum and scalar transport at the turbulent/non-turbulent interface of a jet", *Journal of Fluid Mechanics*, Vol. 631, pp. 199-230.

L. Zhou, W. Zhao, K. H. Luo, H. Wei and M. Xie, 2021, "Spray–turbulence–chemistry interactions under engine-like conditions", *Progress in Energy and Combustion Science*, Vol. 86, pp. 100939.

M. F. Trujillo, S. Gurjar, M. Mason and A. Agarwal, 2018, "Global characterization of the spray formation process", *Atomization and Sprays*, Vol. 28, pp.

J. M. Desantes, R. Payri, F. J. Salvador and A. Gil, 2006, "Development and validation of a theoretical model for diesel spray penetration", *Fuel*, Vol. 85, pp. 910-917.

J. Lee, H. J. Sung and T. A. Zaki, 2017, "Signature of large-scale motions on turbulent/non-turbulent interface in boundary layers", *Journal of Fluid Mechanics*, Vol. 819, pp. 165-187.

K. Chauhan, J. Philip, C. M. De Silva, N. Hutchins and I. Marusic, 2014, "The turbulent/non-turbulent interface and entrainment in a boundary layer", *Journal of Fluid Mechanics*, Vol. 742, pp. 119-151.

G. Borrell and J. Jiménez, 2016, "Properties of the turbulent/non-turbulent interface in boundary layers", *Journal of Fluid Mechanics*, Vol. 801, pp. 554-596.

J. Yang, J. Hwang and H. J. Sung, 2016, "Structural organization of the quiescent core region in a turbulent channel flow", *International Journal of Heat and Fluid Flow*, Vol. 62, pp. 455-463.

D. Mistry, J. Philip and J. R. Dawson, 2019, "Kinematics of local entrainment and detrainment in a turbulent jet", *Journal of Fluid Mechanics*, Vol. 871, pp. 896-924.

J. Hwang and H. J. Sung, 2018, "Wall-attached structures of velocity fluctuations in a turbulent boundary layer", *Journal of Fluid Mechanics*, Vol. 856, pp. 958-983.

J. Hwang and H. J. Sung, 2019, "Wall-attached clusters for the logarithmic velocity law in turbulent pipe flow", *Physics of Fluids*, Vol. 31, pp. 055109.

J. Hwang, J. H. Lee and H. J. Sung, 2020, "Statistical behaviour of self-similar structures in canonical wall turbulence", *Journal of Fluid Mechanics*, Vol. 905, pp. A6.

L. S. Liebovitch and T. Toth, 1989, "A fast algorithm to determine fractal dimensions by box counting", *Physics Letters A*, Vol. 141, pp. 386-390.

F. Moisy and J. Jiménez, 2004, "Geometry and clustering of intense structures in isotropic turbulence", *Journal of Fluid Mechanics*, Vol. 513, pp. 111-133.

M. Holzner and B. Lüthi, 2011, "Laminar superlayer at the turbulence boundary", *Physical Review Letters*, Vol. 106, pp. 134503.

J. Yang, J. Hwang and H. J. Sung, 2019, "Influence of wall-attached structures on the boundary of the quiescent core region in turbulent pipe flow", *Physical Review Fluids*, Vol. 4, pp. 114606.